



 Cite this: *RSC Adv.*, 2024, 14, 15008

# CHN nanocomposites and nanocoating resist enamel white spot lesions by enhancing remineralization and antibacterial activity†

 Lihui Wang,<sup>a</sup> Shuqiang Niu,<sup>b</sup> Shanshan Xu,<sup>b</sup> Yanling Yu<sup>\*b</sup> and Yuanping Hao  <sup>\*b</sup>

Enamel white spot lesions (WSLs) are usually caused by the dissolution of minerals (mainly calcium and phosphate) on the tooth surface due to the acidic environment in the oral cavity. Without timely intervention, WSLs may lead to white spots or a sense of transparency on the tooth surface, and even the formation of dental caries (tooth decay) in severe cases. The key to preventing and treating WSLs is inhibiting the activity of acid-producing bacteria and promoting the remineralization of demineralized enamel. In this study, the network structure formed by sodium tripolyphosphate (TPP) cross-linked chitosan was used to stabilize calcium phosphate, and the multifunctional nanocomposite was constructed by integrating antibacterial components of traditional Chinese medicine, honokiol nanoparticles (HK-NPs) and sodium fluoride to achieve the purpose of resisting cariogenic bacteria and remineralizing with sustained release of calcium and phosphate ions. Notably, we enhanced the remineralization effect of nanocomposites with the help of functional nanocoatings inspired by the mussel biomimetic coating. The experimental results show that the synergistic remineralization effect of nanocomposite and nanocoating is better than that of a single strategy. This multi-prong treatment strategy provides the theoretical and experimental basis for the clinical prevention and treatment of WSLs.

Received 14th February 2024

Accepted 15th April 2024

DOI: 10.1039/d4ra01143k

[rsc.li/rsc-advances](https://rsc.li/rsc-advances)

## 1 Introduction

Dental caries is the most common chronic bacterial infectious disease, which seriously endangers human oral and general health and brings a huge health burden to many countries around the world.<sup>1</sup> Dental caries is a chronic, progressive and destructive disease that occurs in the hard tissues of teeth under the influence of a variety of factors, mainly bacteria.<sup>2</sup> Enamel white spots lesions (WSLs) are the early stage of caries. When cariogenic bacteria metabolize carbohydrates, they create an acidic environment, which leads to demineralization of hard tooth tissues, the formation of enamel white spots, and even caries lesions if left untreated.<sup>3</sup> The risk factors of dental caries include poor oral hygiene, dry mouth caused by eating high-sugar substances, drugs or diseases, *etc.* During the orthodontic process, orthodontic appliances such as brackets and archwires increase the difficulty of cleaning and the incidence of dental caries.<sup>4,5</sup> However, in fact, caries lesions are a process that proceeds alternately with demineralization and remineralization.<sup>6</sup> Destroying the acidic environment or promoting

remineralization can prevent the development of caries and promote the remineralization of demineralized teeth.<sup>7,8</sup> Therefore, the development of a safe and effective system with both antibacterial and remineralizing properties is the key to prevent and stop dental caries.

Biomimetic remineralization technology,<sup>9</sup> a method that mimics the natural mineralization process, has become a development trend in the prevention and treatment of dental caries. Remineralization materials are broadly classified into two categories,<sup>10</sup> fluoride therapies, which strengthen enamel with fluoride and promote mineral deposition,<sup>11–13</sup> and calcium phosphate techniques, which promote remineralization by providing additional calcium and phosphate.<sup>14–17</sup> Studies have applied bioactive glass in combination with chitosan as an alternative therapy to stop the development of dental caries.<sup>18,19</sup> Its caries prevention ability is derived from the calcium ion and phosphate ion provided by bioactive glass and the antibacterial property of chitosan. Bioactive glass (Bglass) is a bioactive glass-based biomaterial that provides calcium and phosphate ions during remineralization and has been demonstrated to have the potential to promote remineralization of early enamel lesions.<sup>20</sup> However, the application of bioactive glasses is limited by the difficulty of controlling the dissolution rate and the possible irritation of surrounding tissues. Chitosan is an N-deacetylated chitin derivative naturally present in arthropod shells.<sup>21</sup> Due to its easy availability, biocompatibility, biodegradability, and non-toxicity, it has received much attention as a functional

<sup>a</sup>School of Shandong Second Medical University, Weifang 261053, Shandong, China

<sup>b</sup>Qingdao Stomatological Hospital Affiliated to Qingdao University, Qingdao 266001, Shandong, China. E-mail: qdkqyyl@163.com; yphao@qdu.edu.cn; Fax: +86-0532-82796465; Tel: +86-186-6195-0867; +86-166-2238-0102

 † Electronic supplementary information (ESI) available. See DOI: <https://doi.org/10.1039/d4ra01143k>


biomaterial.<sup>22</sup> Its high nitrogen content makes chitosan a potential carrier for carrying Ca and phosphate plasma for biomineralization.<sup>23,24</sup> In addition, the positive charge of chitosan can bind to the negatively charged *Streptococcus mutans* and play an antibacterial role by inhibiting the growth of *S. mutans*.<sup>22,25</sup> Calcium phosphate has attracted much attention because it can provide large amounts of  $\text{Ca}^{2+}$ ,  $\text{PO}_4^{3-}$ . Nowadays, a series of novel calcium phosphate-based remineralization delivery systems have been developed for clinical remineralization.<sup>26–28</sup> However, different forms of calcium phosphate have different stability and solubility in the oral environment, and require controlled release through specific carriers.<sup>25,29,30</sup> Therefore, designing a sustained release system is helpful for calcium phosphate to play a better remineralization role. Sodium tripolyphosphate (TPP) is an inorganic compound that has been widely studied for its ability to react with a variety of biopolymer molecules such as chitosan. In these reactions, the negative charge of TPP interacts with the positively charged amino group on the chitosan molecule to form a stable cross-linking network.<sup>31</sup> This process not only enhances the physicochemical stability of the material, but also enables the control of drug release rate, making it an important application in biomedicine and drug delivery systems.<sup>32–34</sup>

The key to prevent the occurrence and progression of dental caries is to inhibit cariogenic bacteria and promote remineralization.<sup>35</sup> There is no doubt that the enamel biomimetic reconstruction system combined with the antibacterial idea will be more effective. Oral antimicrobial agents (chlorhexidine, metronidazole, roxithromycin, *etc.*) affect the normal oral flora, destroy the ecological balance, and cause bacterial resistance.<sup>36</sup> In recent years, traditional Chinese medicine (TCM) has received extensive attention due to its low side effects, and natural antibacterial agents have been explored. Honokiol (HK) is a natural antibacterial agent extracted from *Magnolia officinalis*.<sup>37,38</sup> HK showed significant antibacterial activity against both Gram-positive and Gram-negative bacteria, especially against *S. mutans*. Honokiol is not easy to produce bacterial resistance, and has a wider range of antibacterial properties.<sup>38–41</sup> However, the inaqueous solubility of honokiol reduces its bioavailability. Recent advances in nanoparticle technology are addressing this challenge.<sup>42–44</sup>

In recent years, significant progress has been made in integrating functional coatings into biomimetic enamel reconstruction systems. Dopamine and metal phenol coatings have received much attention due to their outstanding adhesion properties. Dopamine (DA) is a common catechol-like neurotransmitter. A series of reactions occur in an alkaline environment to form polydopamine films, which can adhere to the surface of any fixed material with good adhesion and induce the deposition of hydroxyapatite.<sup>45,46</sup> Alternatively, inspired by the adhesive properties of mussel polyphenols, polyphenolic substances have been identified as ideal intermediate molecules to link inorganic and organic phases. Multifunctional functional metal-phenol networks (MPNS) have been developed by exploiting the different chelating abilities of phenolic materials and metal ions. They are used to modify or coat inorganic and metallic surfaces, thereby promoting

hydroxyapatite crystallization, biomineralization, bone regeneration, and cell adhesion. For example, after deposition of tannin- $\text{Fe}^{3+}/\text{Cu}^{2+}$  complexes, calcium and phosphate ions can be attracted from natural saliva to promote the remineralization of hydroxyapatite crystals.<sup>47,48</sup>

In summary, we fabricated a network structure consisting of TPP and chitosan to stabilize calcium and phosphate ions in calcium phosphate, introduced honokiol nanoparticles to enhance the material's inhibition against cariogenic bacteria, and added sodium fluoride to enhance enamel remineralization nanocomposites (CHN). The anti-biofilm activity and enamel remineralization activity were evaluated *in vitro*. At the same time, the combination of nanocoatings prolongs the action time and efficiency of nanocomposites. CHN nanocomposites combined with nanocoatings have great clinical potential to effectively halt the cariogenic process and prevent dental caries.

## 2 Materials and methods

### 2.1 Materials

Honokiol (purity = 98.5%), bovine serum albumin (96–99%) (BSA), polyvinylpyrrolidone (PVP 9003-39-8 average mol wt 40 000), and acetone, chitosan (MW 100000–350000), calcium dichloride ( $\text{CaCl}_2$ ), acetic acid, di-potassium hydrogen phosphate ( $\text{K}_2\text{HPO}_4$ ), and sodium tripolyphosphate (TPP) were purchased from Sigma-Aldrich. Fetal bovine serum (FBS) and penicillin-streptomycin, artificial saliva, KOH, NaF, thymol, 75% ethanol, 10% CCK-8 culture medium,  $\text{FeCl}_2 \cdot 4\text{H}_2\text{O}$ ,  $\text{CuCl}_2 \cdot 2\text{H}_2\text{O}$ , tannic Acid (TA), tris buffer, 37% phosphoric acid, Baclight Live/Dead Bacterial Viability Assay Kit (Molecular Probes, Eugene, OR, USA), crystal Violet (CV) staining solution were purchased from Macklin Reagent Co. Ltd (Shanghai, China), Brain Heart Infusion Broth (BHI), Trypticase (Tryptic) Soy Broth (TSB), Lysogeny Broth (LB) broth, Nutrient Agar were purchased from Macklin Reagent Co. Ltd (Shanghai, China). All reagents were used as received without further purification.

### 2.2 Synthesis of honokiol-loaded nanoparticles (HK-NPs)

HK-NPs were synthesized using the liquid antisolvent precipitation method.<sup>43</sup> In this process, 10 mg BSA and 10 mg PVP were dissolved in 4 mL deionized water at room temperature as stabilizers to form a water phase. Subsequently, HK 20 mg was dissolved in 0.8 mL acetone to form the oil phase, and then the oil phase was slowly and evenly added to the water phase under ultrasonic wave. HK-NPs was obtained after acetone was removed by spin evaporation with a rotary evaporator.

### 2.3 Load capacity and encapsulation efficiency calculation

UV-vis spectrophotometry (Bio-DL, USA) was used to detect the loading capacity (LC) and encapsulation efficiency (EE) of HK-NPs according to a standard curve method. Briefly, the prepared HK-NPs were centrifuged at a high speed of 5000 rpm for 15 min. After centrifugation, the supernatant was collected and an aqueous acetonitrile solution was added to the precipitate and washed three times. The last obtained precipitation is freeze-



dried for further use. The supernatant was collected and the amount of honokiol neutralized in the supernatant was detected by UV. The LC and EE are calculated by the following formula:

$$\text{LC}(\%) = \frac{\text{Weight of HK in NPs}}{\text{Weight of NPs}} \times 100\%$$

$$\text{EE}(\%) = \frac{\text{Weight of HK in NPs}}{\text{Weight of HK}} \times 100\%$$

## 2.4 *In vitro* release behavior

The *in vitro* release of honokiol from the nanoparticles was analyzed using dialysis bag diffusion in artificial saliva, PBS (pH 5.5), PBS (pH 7.4) and artificial saliva (pH 6.5–7.0) with 0.5 wt% sodium dodecyl sulfate (SDS). 1 mg mL<sup>-1</sup> HK-NPs were placed in dialysis bags (MwCO 3500) and incubated in 50 mL of release medium at 37 °C with constant shaking at 120 rpm. Samples (3 mL) were withdrawn at specified intervals up to 72 h and replaced with an equal amount of fresh medium to maintain sink conditions. The drug release was quantified using a UV spectrophotometer, and cumulative drug release was calculated, with each sample analyzed in triplicate.

## 2.5 Synthesis of Chi-CaP/HK-NPs/NaF nanocomposites (CHN)

Chitosan microgel was synthesized using the ionotropic gelation method.<sup>29</sup> (i) Briefly, chitosan (0.175 w/v%) was dissolved in 1% acetic acid, and the pH was adjusted to 4.76 using 10 M KOH with agitation at 100 rpm. To this solution, 10 mL of 0.46 M CaCl<sub>2</sub> was added under similar conditions.

(ii) TPP solution (0.29 w/v%) was prepared by mixing TPP in 10 mL of 0.282 M K<sub>2</sub>HPO<sub>4</sub>. 10 mL of TPP solution was added to (i) and stirred at 500 rpm continuously until an opalescence appeared, indicating the formation of Chi-CaP (chitosan-calcium phosphates). Different amounts of HK-NPs and NaF (3900 ppm) were mixed with the chitosan microgel, designated as Chi-CaP/HK-NPs/NaF nanocomposites (CHN nanocomposites). According to the description of the antibacterial concentration of HK in the existing literature<sup>40</sup> and the study of the antibacterial concentration of HK-NPs, the concentration of HK-NPs in the experiment was 50, 100 and 500 µg mL<sup>-1</sup>, respectively, named CHN-1, CHN-2 and CHN-3, respectively.

## 2.6 Characterization of HK-NPs and CHN nanocomposites

The size and shape of HK-NPs and CHN nanocomposites were determined by transmission electron microscopy (TEM, JEM-2100UHR, JEOL, Japan). The zeta potential was determined using dynamic light scattering (DLS, Malvern instrument, England). Fourier transform infrared (FTIR) spectroscopy analyses of CS, Chi-CaP, CHN nanocomposites, HK, and HK-NPs in the range of 500–4000 cm<sup>-1</sup> were performed with an attenuated total reflectance-infrared (ATR-IR) system by a Nicolet iN10 FTIR spectrometer (ThermoFisher Scientific, Waltham, MA, USA).

## 2.7 Remineralization of demineralized enamel lesions

**2.7.1 Demineralization of enamel specimens.** All isolated teeth were obtained from Qingdao Stomatological Hospital and approval was provided by the Ethics Committee of Qingdao Stomatological Hospital (2023KQYX028). The enamel of a healthy adult third molar was taken without caries, cracks or defects, and all soft tissues, dental stones and pigments were removed. After mechanical cleaning, the crown is cut into enamel pieces with emery along the bucco-lingual surface. The blocks were then ultrasonic cleaned in pure water for 30 min, and rinsed in 75% ethanol. The enamel sample was etched with 37% phosphoric acid for 30 s to form a demineralized model, which was then extensively rinsed with deionized water and ultrasound and stored in 0.1% thymol solution at 4 °C for further use.

**2.7.2 Different tooth surface coating treatments.** Tannic acid (TA)–Fe<sup>II</sup> coating<sup>47</sup>: The cleaned dental flakes were immersed in tris buffer (pH = 8) containing FeCl<sub>2</sub>·4H<sub>2</sub>O (0.074 mg mL<sup>-1</sup>) and TA (0.4 mg mL<sup>-1</sup>). After 12 h, the flakes were ultrasonically washed with deionized water and dried to form a TA–Fe<sup>II</sup> coating.

TA–Cu<sup>II</sup> coating<sup>48</sup>: The cleaned dental flakes were immersed in tris buffer (pH = 8) containing CuCl<sub>2</sub>·2H<sub>2</sub>O (0.4 mg mL<sup>-1</sup>) and TA (0.25 mg mL<sup>-1</sup>). After 12 h, the flakes were ultrasonically washed with deionized water and dried to form a TA–Cu<sup>II</sup> coating.

Polydopamine coating<sup>45</sup>: Dental flakes were immersed in tris buffer (pH = 8) containing dopamine (2 mg mL<sup>-1</sup>). After 24 h, the treated flakes were ultrasonically washed with deionized water and dried to form a PDA coating.

**2.7.3 Study on *in vitro* remineralization of demineralized enamel.** This study evaluated the effect of CHN nanocomposites on promoting remineralization of demineralized teeth. First, all the enamel plates are soaked in deionized water for 30 min, gently rinsed, and then dried. Each disk was soaked in a solution corresponding to a different treatment group (*n* = 3) consisting of a control group (artificial saliva), Chi-CaP, Chi-CaP + NaF, and CHN nanocomposites. The remineralization process was simulated over 6 h to simulate overnight remineralization. After incubation, the specimen was rinsed with water, soaked in 1 mL synthetic saliva, and kept at 37 °C for 18 h, and the medium was updated daily. After a week of circulation, the specimens were thoroughly rinsed with deionized water and air-dried at 25 °C for analysis. Surface morphology was detected by scanning electron microscopy (SEM, Zeiss, Germany), elemental analysis was performed by energy dispersions X-ray spectroscopy (EDS), and crystal orientation and minerals on the surface of newly formed enamel were analyzed by X-ray diffractometry (XRD, Rigaku Corporation, Japan).

## 2.8 Antibacterial and Antibiofilm performance

**2.8.1 Bacterial culture.** An isolated *S. mutans* colony was cultured in BHI broth until reaching the mid-log phase at 37 °C in a shaker incubator (120 rpm). *E. coli* and *S. aureus* were similarly prepared using LB broth and TSB broth, respectively.



**2.8.2 Planktonic bacterial viability study.** The colony forming unit (CFU) method was used to evaluate the antibacterial effect of CHN nanocomposites on several common cariogenic bacteria, including *S. mutans*, *E. coli*, and *S. aureus*. Different samples (0.2 mL,  $n = 3$ ) were cultured with bacterial solution ( $10^6$  CFU mL<sup>-1</sup>, 1 mL) at 37 °C and 150 rpm for 12 h. Dilute the bacterial solution of each group to coat the plate. The group without adding materials was used as the blank control group. After the agarose plate was incubated in a 37 °C bacterial incubator for 18 h, the CFU on the plate was recorded with a digital camera. The antibacterial rate was calculated by the following formula:

$$\text{Bactericidal rate} = \frac{\text{Control CFU} - \text{Treatment CFU}}{\text{Control CFU}} \times 100\%$$

**2.8.3 The capability of CHN nanocomposites to destroy biofilm.** Live/dead staining and crystal violet (CV) staining assays were conducted to assess the ability of the nanocomposites against biofilms. The prepared *S. mutans* was added to the BHI medium. Incubate at 37 °C for 36 h, changing the medium every 12 h. *E. coli* and *S. aureus* biofilms were prepared by the same method. Chi-CaP/NaF and CHN ( $n = 3$ ) were co-cultured with biofilms, respectively. After incubation at 37 °C for 24 h, they were gently washed with PBS and stained with Live/Dead kit according to the work instructions. The biofilm of each group was observed by a laser confocal microscope. In addition, the micromorphology of the biofilm was observed by SEM (Zeiss, Germany). First, after incubation at 37 °C for 24 h, the above-treated bacteria biofilms were rinsed twice with PBS and then fixed at room temperature with 2.5% glutaraldehyde solution for 8 h. After fixation, the sample was continuously dehydrated with gradient ethanol solutions (30%, 50%, 70%, and 100%). After that, the bacteria were dried on the silicon wafer, sprayed with gold, and then observed with the SEM.

Subsequently, the biofilms treated with Chi-CaP/NaF and CHN were further examined by crystal violet (CV) staining. Each group was added with 300  $\mu$ L of 0.1% CV solution, incubated at room temperature for 15 min, and then gently washed with PBS. Then, anhydrous ethanol was added and treated for 15 min. The absorbance at 570 nm was recorded with a microplate reader (Bio-TEK, USA).

## 2.9 Toxicity of *in vitro* and *in vivo* CHN nanocomposites

**2.9.1 Mammalian cell culture.** Human oral keratinocytes (HOK) (purchased from Wuhan Pricella, China) were cultured in Dulbecco's Modified Eagle Medium (DMEM) supplemented with 10% fetal bovine serum and 1% antibiotic/antimycotic solution, maintained at 37 °C in a humidified atmosphere with 5% CO<sub>2</sub>.

**2.9.2 Biocompatibility *in vitro* assessment.** Cell proliferation was detected with the CCK-8 kit. HOK cells were inoculated on 96-well plates at a density of  $1 \times 10^4$  cells per well. The prepared CHN-3 is then added to the well at different concentrations ( $n = 5$ ) of 5, 10, 15, 20, and 25% (w/v), respectively. After incubating for 24 h, carefully replace the medium with 10%

CCK-8 working solution. After incubation for 4 h, the absorbance at 450 nm was detected.

Biocompatibility of CHN nanocomposites was determined by living/dead cell viability. PBS, CHN-2 and CHN-3 were added to the cells in the above prepared 96-well plates ( $n = 3$ ), cultured for 24 h, and then stained with live/dead staining kit for 0.5 h without light. The cell viability of each group was observed by laser confocal microscopy.

**2.9.3 Biocompatibility *in vivo* assessment.** 4 weeks-old male rats (170–220 g) were selected ( $n = 3$ ) to evaluate the toxicity of the nanocomposites.<sup>49</sup> These animal experiments were approved by the Ethics Committee of Qingdao Stomatological Hospital (2023KQYX027) and complied with the regulations on the management of experimental animals. The control group was given single steaming water. The treatment group was given CHN-2 nanocomposites and CHN-3 nanocomposites, respectively, and one week later, the rats were euthanized and their major organs were pathologically analyzed. Blood was collected by cardiac puncture for hematological and biochemical analysis. The heart, liver, spleen, lung, and kidney were taken, and fixed with 10% formalin, then pathological sections were taken, and hematoxylin and eosin (H&E) staining were used for histological evaluation.

## 2.10 Statistical analysis

All data are expressed as means standard deviations of values from three independent experiments. One-way analysis of variance and *t*-tests were used to analyze the differences between the experimental groups. Statistical significance was set at 0.05 (\* $p < 0.05$ , \*\* $p < 0.01$ , \*\*\* $p < 0.001$ ).

# 3 Results and discussion

As shown in Fig. 1, this paper designed a network structure formed by TPP linked chitosan to stabilize calcium ions and phosphate ions, and assembled HK-NPs and sodium fluoride to construct a multifunctional nanocomposites (CHN). The remineralization effect was improved by nanocoating. The remineralization and antibacterial properties of the nanocomposites were verified by remineralization experiment and bacterial experiment *in vitro*.

## 3.1 Synthesis and characterizations of CHN nanocomposites

Honokiol (HK) nanoparticles were synthesized by the method previously reported.<sup>42</sup> Firstly, HK-NPs were prepared by combining PVP and BSA as colloidal stabilizers with HK in acetone solution to improve their water solubility. Drug loading is an important index to measure the drug-loading ability of nanoparticles.<sup>50</sup> The drug loading rate of HK-NPs was  $74.65 \pm 0.47\%$  and the encapsulation rate was  $92.86 \pm 0.28\%$ , which indicated that there was a certain drug loss during the preparation of nanoparticles.

The morphology of HK-NPs was observed by TEM (Fig. 2a). The nanoparticles were well dispersed and regularly spherical, with an average diameter of about 229.8 nm. The specific distribution of these nanoparticles is known through Fig. S1





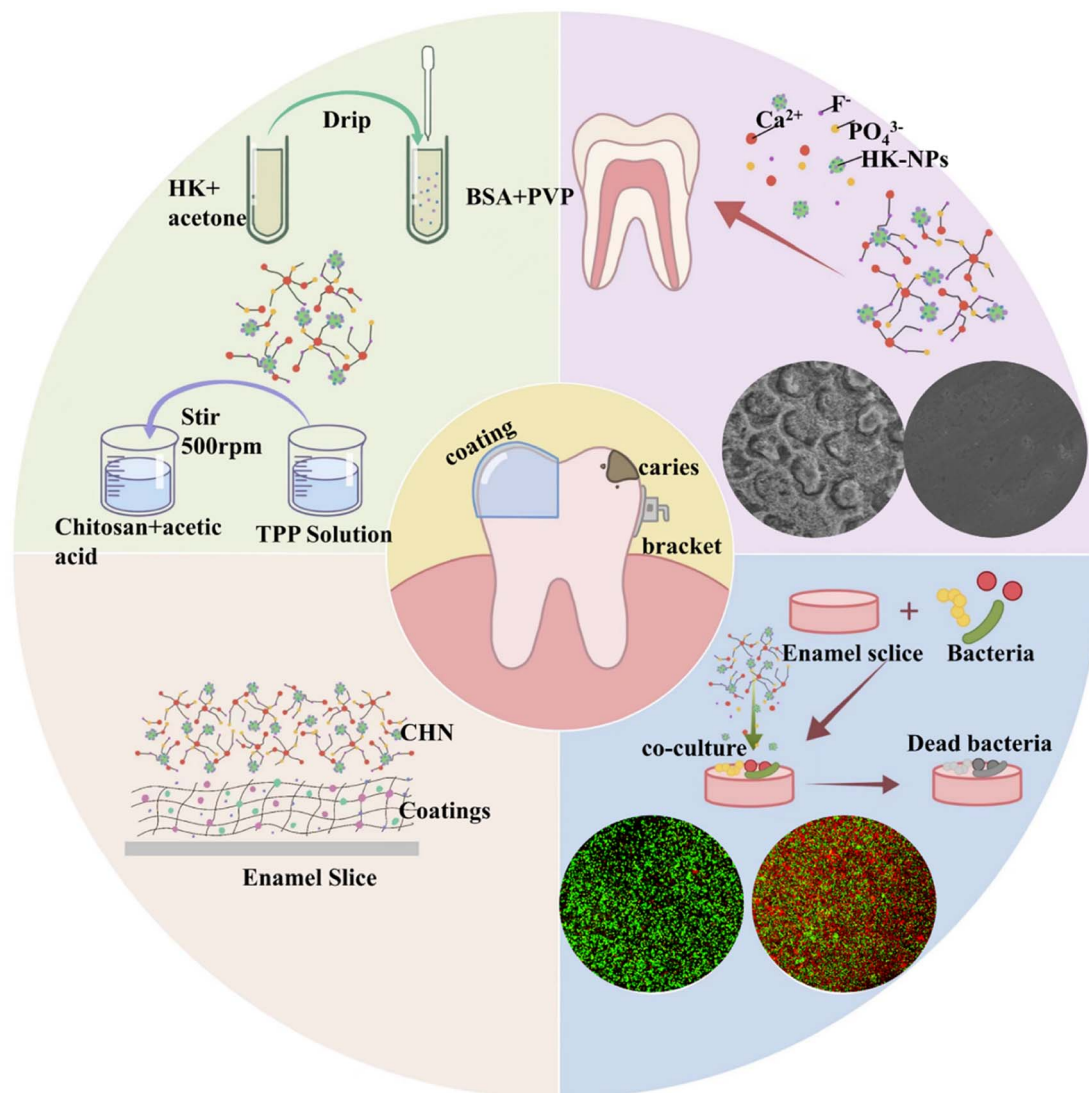


Fig. 1 The top left corner illustrates the formation process of honokiol nanoparticles and Chi-CaP. The top right corner depicts how CHN nanocomposites facilitate dental remineralization. The bottom left corner demonstrates the functional mechanism of the dental surface coating. The bottom right corner represents the antibacterial process.

ESI.† HK-NPs are unimodal and have a narrow size distribution (0.170). To demonstrate the synthesis of HK-NPs, we used FT-IR to detect the composition of chemical groups of HK-NPs. Fig. 2b shows the FT-IR spectra of HK and HK-NPs. The characteristic peaks of HK can be seen at  $3300\text{ cm}^{-1}$  (hydroxyl stretching vibration),  $3000\text{ cm}^{-1}$  (aromatic ring C-H vibration),  $1500\text{ cm}^{-1}$  (aromatic ring C=C vibration) and  $1000\text{ cm}^{-1}$  (ether bond C-O vibration) in the HK-NPs spectrum. Furthermore,  $1650\text{ cm}^{-1}$  is kicked up by the amide group vibration in PVP, and at  $1540\text{ cm}^{-1}$  (a combination of N-H bending vibration and C-N stretching vibration) is the characteristic peak of the amide II band.<sup>39</sup> At the same time, there are characteristic peaks of the amide II band (a combination of N-H bending and C-H stretching vibrations).<sup>50,51</sup> The above characterization proves the successful synthesis of HK-NPs. The acidic environment in the mouth where cariogenic bacteria break down carbohydrates can lead to tooth demineralization.<sup>52</sup> We therefore examined the

release kinetics of HK-NPs in PBS solutions (pH 5.5 and 7.4) and artificial saliva (pH 6.5–7.0). As expected, the release of HK-NPs at  $37\text{ }^{\circ}\text{C}$  for 72 h was time- and pH-dependent. As can be seen from the release curve in Fig. 2c, HK releases the fastest in pH 5.5 environment. The release rate was about 55% at 12 h and up to 80% at 72 h, while the release rate of HK was relatively low in neutral PBS and artificial saliva. This indicates that HK-NPs has stronger antibacterial ability in caries causing environment.

Fig. 2d shows the chemical equation involved in the experimental reaction. Chitosan dissolves under acidic conditions, the amino group in chitosan is converted to  $\text{NH}_3^+$ , and then the excess acetic acid is neutralized with KOH, and a more nanocomposites chemical reaction occurs after adding calcium chloride, which can be simplified as calcium ions and ions on chitosan combine to form a stable network structure. The polyvalent anions in TPP can be cross-linked by amino groups on chitosan to form gel particles. This is the structural basis of



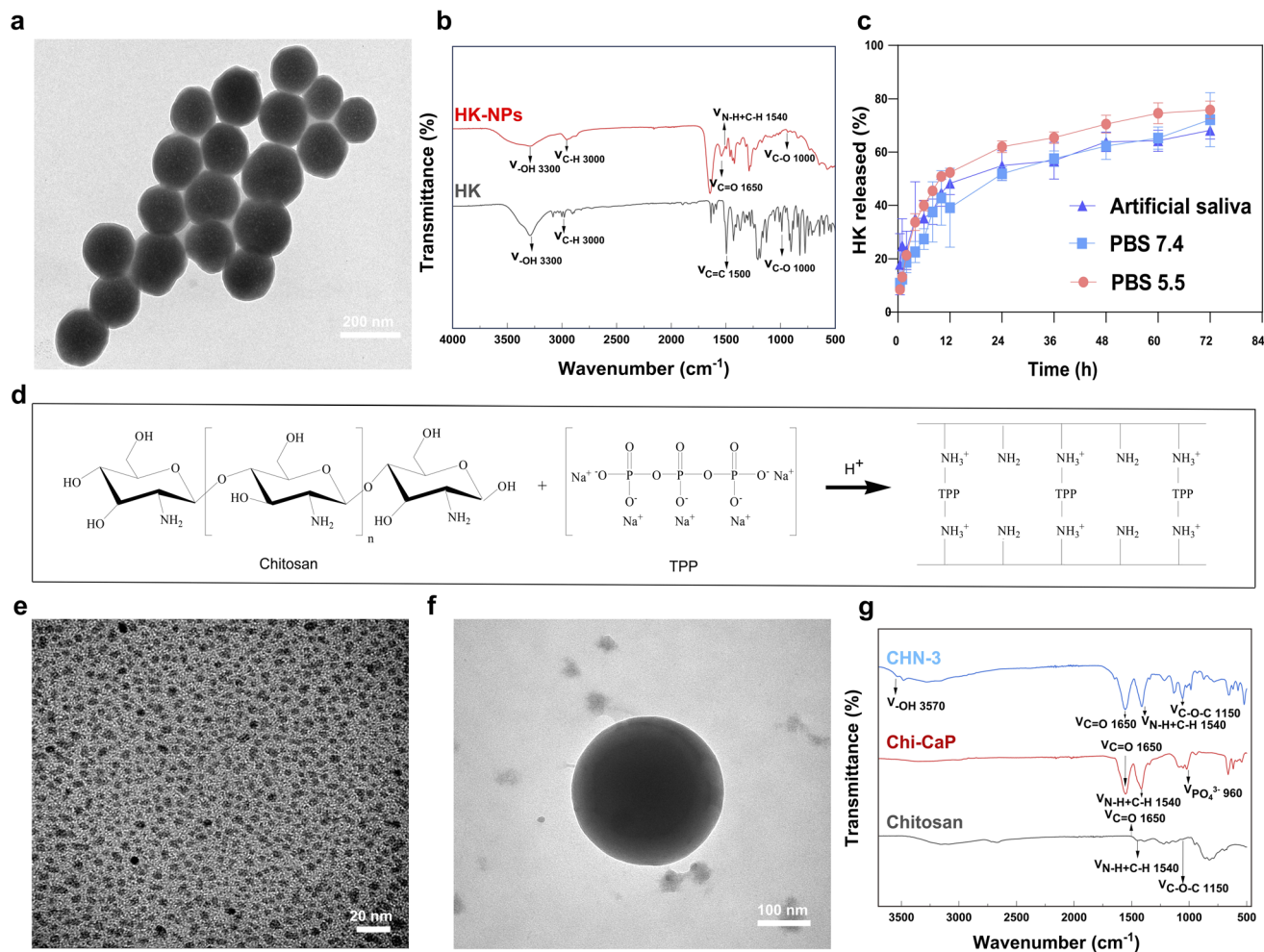


Fig. 2 Characterizations of HK-NPs and CHN nanocomposites. (a) Transmission electron microscopy (TEM) image of HK-NPs. (b) Fourier-transform infrared (FTIR) spectroscopy of HK and HK-NPs. (c) The drug release profile of HK-NPs over 72 h at pH 5.5, pH 7.4, and in artificial saliva. (d) Chemical equations involved in the synthesis of CHN nanocomposites. (e) TEM images of Chi-CaP and (f) CHN nanocomposites. (g) FTIR spectroscopy of chitosan, Chi-CaP and CHN-3.

the formation of chitosan-calcium phosphate microgels. Phosphate ions and calcium ions form calcium phosphate and finally form the chitosan-calcium phosphate nanocomposites.

The Chitosan (Chi)-CaP was synthesized through ionotropic gelation. In Fig. 2e, The TEM imaging of the Chi-CaP revealed uniformly dispersed, near-spherical CaP nanoparticles within the chitosan matrix. These nanoparticles exhibited an average diameter of approximately 2 nm, and their zeta potential was measured to be  $21.4 \pm 0.304$  mV. In Fig. 2f, the TEM imaging of the CHN nanocomposites revealed HK-NPs is dispersed in Chi-CaP, proving that CHN is a stable system. Further elucidate the molecular and functional group changes during the synthesis of CHN nanocomposites by FTIR. The FTIR of chitosan, Chi-CaP composites, and CHN nanocomposites in Fig. 2g demonstrated distinctive bands, reflective of their molecular structures. In the case of chitosan, the absorption band near  $1650\text{ cm}^{-1}$  corresponds to the amide I band and originates mainly from C=O stretching vibrations. Furthermore, the band observed near  $1540\text{ cm}^{-1}$  is attributed to the combination of N-H bending vibrations and C-N stretching vibrations, which are characteristic

of the amide II band. In addition,  $1150\text{ cm}^{-1}$  is a C-O-C stretching vibration, representing the skeleton vibration in the chitosan molecular chain. Chi-CaP spectra show additional peaks, especially around  $960\text{ cm}^{-1}$ , attributed to the inherent P-O stretching vibrations of CaP. This particular band signals the successful integration of CaP within the composite material. The intensity and a slight shift in this band within the composite may be interpreted as evidence of interaction between CaP and the chitosan matrix. Notably, the peak around  $3570\text{ cm}^{-1}$  observed in the components' spectrum is suggestive of O-H stretching, possibly resulting from the hydration of the HK-NPs.

In conclusion, the comprehensive analysis using FTIR spectroscopy, alongside TEM, dynamic light scattering, and zeta potential assays, collectively confirms the successful synthesis of CHN nanocomposites.

### 3.2 Evaluation of antimicrobial performance of CHN nanocomposites

**3.2.1 Evaluation of the performance against planktonic bacteria.** To verify the antibacterial effect of CHN on common



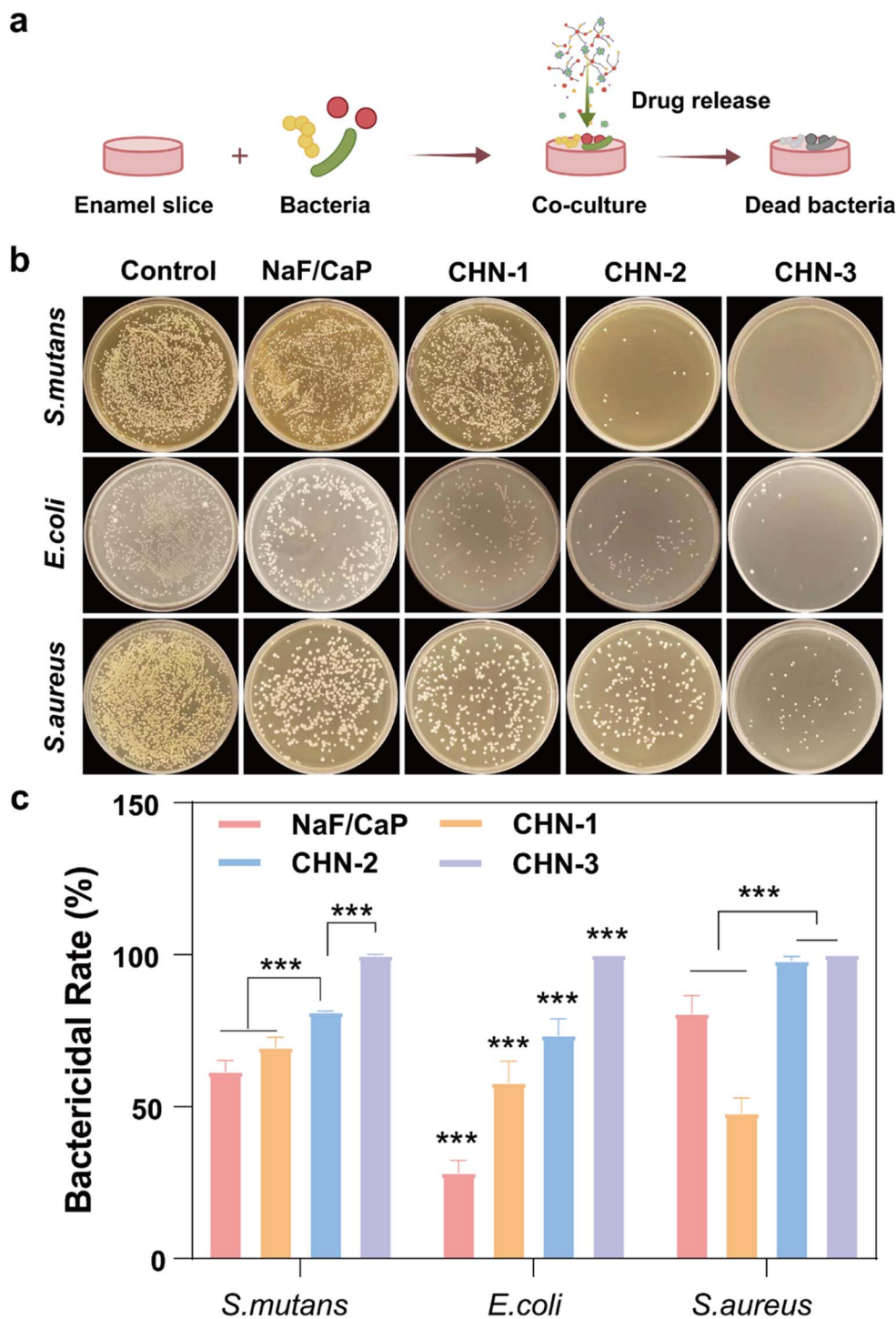


Fig. 3 Evaluation of the antibacterial properties of the CHN nanocomposites. (a) Schematic representation of the antimicrobial properties of CHN nanocomposites. (b) Agar plates of *S. mutans*, *E. coli*, and *S. aureus*, post-treatment with PBS, NaF/CaP and different CHN samples. (c) Bactericidal rate of the on *S. mutans*, *E. coli*, and *S. aureus*, NaF/CaP and different CHN samples on *S. mutans*, *E. coli*, and *S. aureus*.

oral pathogens, *S. mutans*, *E. coli*, and *S. aureus* were selected as model bacteria. The antibacterial activity of CHN against three planktonic bacteria was verified by plate counting method. In Fig. 3b and c, NaF/CaP had certain antibacterial effect on *S. mutans* and *S. aureus*, with the antibacterial rate of 65.38% and 77.4%, while it had no obvious antibacterial effect on large

intestine, with the antibacterial rate of 29.82%. The antibacterial properties were significantly enhanced by the addition of HK-NPs, which may be due to the destruction of the biofilm of the bacteria and the interference of the synthesis of key substances to interfere with the growth and reproduction of the bacteria.<sup>38</sup> CHN-3 had significant antibacterial activity against





the three types of bacteria, and the bactericidal rate was close to 100%. Therefore, based on the balance between bactericidal ability and biocompatibility, CHN-3 was used in subsequent experiments.

**3.2.2 Evaluation of anti-biofilm performance.** In this study, *S. mutans*, *E. coli*, and *S. aureus* were selected as representative strains to establish a biofilm model closely related to enamel WSLs. The anti-biofilm performance of CHN was evaluated using live/dead bacterial viability reagents (Fig. 4a). Green means live bacteria, and red means dead bacteria. The enamel

surface of the control group showed green fluorescence and a small number of red spots in NaF/CaP, indicating that NaF/CaP had weak anti-biofilm effect, while the CHN-3 group showed almost all red fluorescence, indicating that CHN-3 had excellent anti-biofilm activity. The microscopic morphology of biofilm co-cultured with materials was further observed by SEM. As can be seen from Fig. 4b in the control group, *S. mutans*, *E. coli*, and *S. aureus* have intact morphology and smooth surfaces. Only a few biofilms were incomplete in the NaF/CaP group. However, the surface of the bacteria in CHN is severely

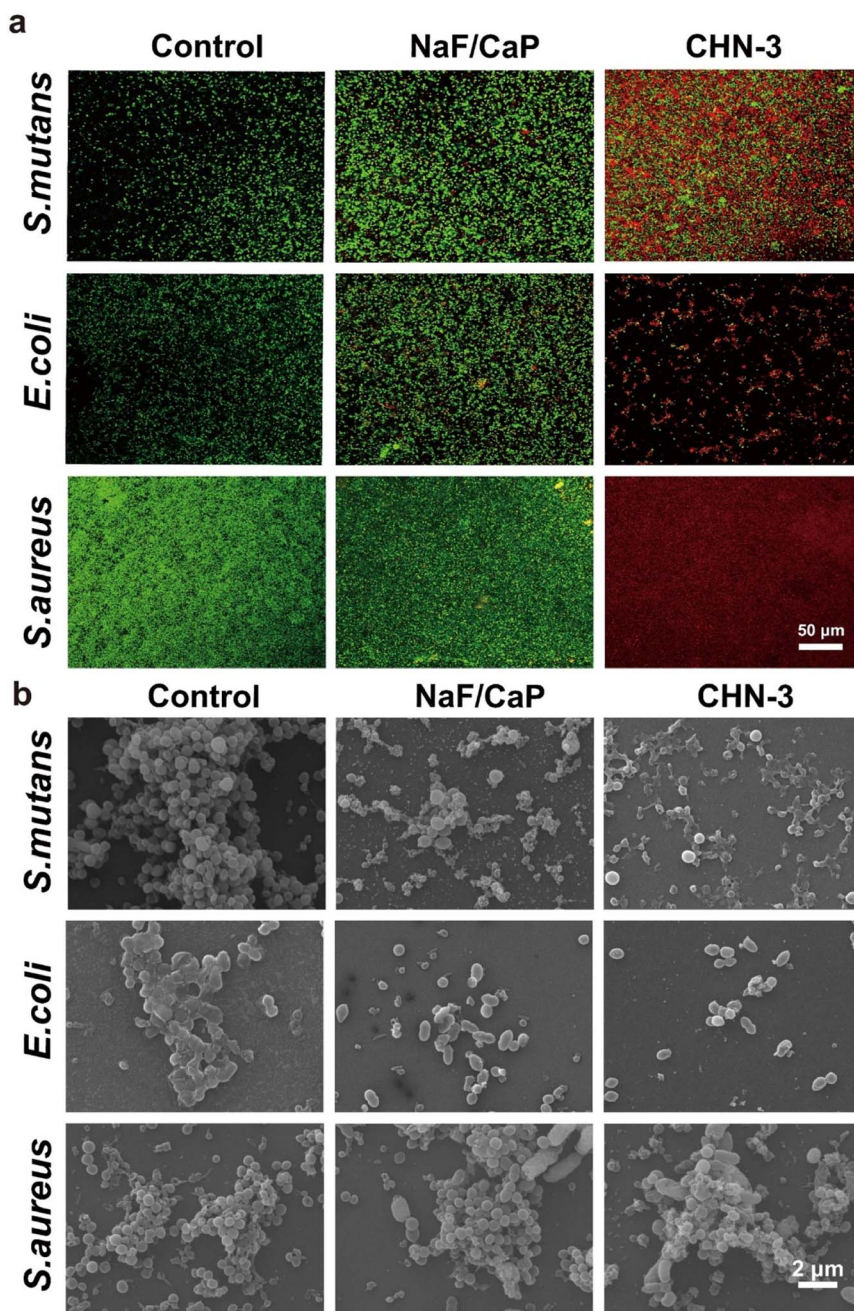


Fig. 4 (a) Depicts CLSM images after a 48 hours culture of *S. mutans*, *E. coli*, and *S. aureus*. These cultures were subsequently co-incubated for 24 h with PBS (control group), NaF/CaP, and CHN. (b) SEM images of biofilms from *S. mutans*, *E. coli*, and *S. aureus* after various treatments.





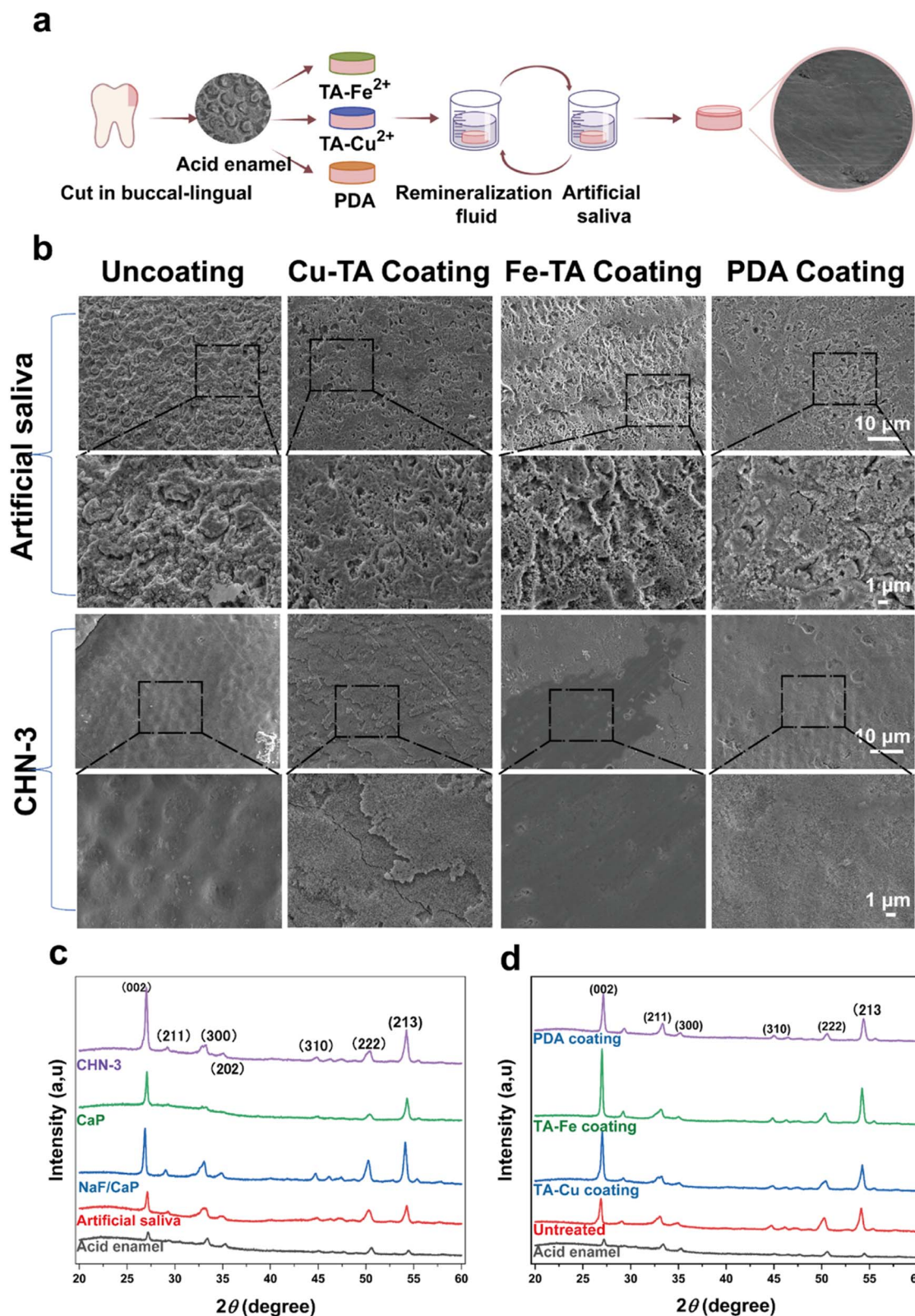


Fig. 5 Evaluation of the remineralization capabilities of CHN nanocomposites. (a) The diagram of the remineralization process. (b) Uncoated, Fe-TA/Cu-TA and PDA-coated demineralized enamel treated with artificial saliva and CHN-3 for 7 days by SEM. (c) XRD patterns of acid enamel, artificial saliva, CaP, NaF/CaP and CHN-3 treated demineralized enamel. (d) XRD pattern of demineralized enamel treated with TA-Cu, TA-Fe and PDA coating and then treated with CHN-3 for 7 days.



wrinkled, the morphology is incomplete, and the surface biofilm is damaged, demonstrating that CHN-3 can cause effective destruction of the biofilm. In Fig. S2a ESI† little biofilm was seen in the CHN-3 group, and a large number of biofilm was formed in the control group and the NaF/CaP group. At the same time, the biofilm content measured by 570 nm absorbance showed that CHN-3 had prominent biofilm inhibition effect. This is consistent with the above results (Fig. S2b, ESI†). All the results showed that CHN had better antibacterial activity and biofilm inhibition ability.

### 3.3 Evaluation of remineralization

The synergistic effect of CHN nanocomposite with three coatings on enamel mineralization was investigated using an *in vitro* demineralized enamel model. SEM was used to observe the surface morphology of enamel in each group (Fig. 5a and S3 ESI†). After 37% phosphoric acid corrosion, the enamel developed a “fish scale” appearance and exposed enamel prismatic structure (Fig. S3 ESI†). In the uncoated group, the typical morphology of the acid-etched enamel surface could still be seen after the demineralized enamel block was immersed in artificial saliva for 7 days, illustrating the necessity of using a remineralizing agent. The degree of remineralization was similar between the NaF/CaP and CHN-3 groups (Fig. S3 ESI†), indicating that the addition of HK-NPs did not affect the remineralization of the material. The degree of remineralization in the NaF/CaP and CHN-3 groups was significantly higher than that in the artificial saliva and Chi-CaP groups, and HAP crystal deposition was evident between enamel prism structure. This result illustrates the ability of CHN nanocomposites to promote remineralization. However, the uncoated enamel blocks treated with CHN-3 retained the outline of the enamel prism structure (Fig. 5b). Inspired by the bioadhesion of mussels in nature, nanocoatings were used to increase the interaction time of CHN complex on the tooth surface to improve the remineralization effect. The effects of dopamine and metallophenol on enamel remineralization have been investigated.<sup>46–48</sup> PDA coating and TA-Fe and TA-Cu coating were prepared on the demineralized tooth surface, and after CHN-3 treatment, dense and ordered rod-like mineral crystals were formed on the enamel surface without obvious outline of the enamel prism-like structure (Fig. 5 and S3 ESI†). Under the magnification of x3000, the deposited crystal particles can be observed in the TA-Cu and PDA groups, and the HAP crystal layer of the TA-Fe group is denser. X-ray diffraction analysis was used to identify the types of crystals formed on the enamel (Fig. 5c and d). As shown in Fig. 5c, (002), (211), (300), (222), and (213) have distinct HAP diffraction peaks at  $2\theta = 25.9^\circ$ ,  $31.8^\circ$ ,  $32.8^\circ$ ,  $46.7^\circ$ , and  $49.5^\circ$ . After acid etching, the characteristic peaks of (002), (211), (300), (222) and (213) were weakened or disappeared. The recovery of these peaks after CHN-3 and coating treatments indicated the formation of crystalline HAP, indicating the outstanding remineralization promoting properties of the CHN nanocomposites. Fig. 5d shows that after CHN treatment, compared with the uncoated group, the relative intensity of HAP characteristic peaks in the PDA coated group

**Table 1** Calcium–phosphorus ratios obtained by EDS assay of dentinal surfaces with different coatings treated with artificial saliva

	Uncoating	Cu-TA coating	Fe-TA coating	PDA coating
Ca	24.38	30.59	36.4	34.89
P	14.33	17.29	19.07	19.5
Ca/P	1.701	1.769	1.908	1.789

**Table 2** Calcium–phosphorus ratios obtained by EDS assay of dentinal surfaces with different coatings treated with CHN-3 nanocomposites

	Uncoating	Cu-TA coating	Fe-TA coating	PDA coating
Ca	40.99	34.66	47.68	41.12
P	21.71	19.08	23.44	22.06
Ca/P	1.88	1.816562	2.034	1.86

and TA-Fe coated group increased, and the TA-Fe coated group increased more, indicating that the CHN nanocomposite formed HAP crystal phase in the TA-Fe coated group had higher content and the best remineralizing performance. The Ca/P value of natural enamel is close to Hap (1.67),<sup>53</sup> the standard chemical measure. Energy dispersive X-ray spectroscopy (EDS) (Tables 1 and 2, Fig. S4 ESI†) showed that the ratio of Ca to P in the remineralization layer increased. Compared with the ratio of Ca to P after acid etching, the ratios of Ca to P in the TA-Cu group, TA-Fe group and PDA group were 1.8, 2.0, and 1.86, respectively, which further confirmed that CHN-3 could play a better remineralization role under the synergic action of the coating. Overall, the results show that the CHN nanocomposites have good remineralization properties under the synergistic action of the coatings and are critical for practical and clinical applications.

### 3.4 Cytocompatibility evaluation

A live/dead cell viability assay and CCK-8 kit assay were conducted to measure the influence of CHN on HOK cells viability after being cocultured for 24 h, and the cytotoxicity was negligible (Fig. 6a and b). Rats treated with CHN were closely monitored and recorded to assess the biosafety of CHN, and no adverse reactions occurred in the experimental group, as in the control group. CHN materials can accumulate in different organs through the digestive and blood circulation systems, which can also lead to unexpected toxicity. However, studies comparing hematological parameters in serum, including blood biochemical parameters such as alanine aminotransferase (ALT), aspartate aminotransferase (AST), and URE showed no significant difference between the control and experimental groups (Fig. 6c). Hematoxylin-eosin (H&E) staining of major organs (heart, liver, spleen, lungs, kidneys) did not reveal any significant signs of degeneration, necrosis, or toxicity (Fig. 6d), indicating the safety of CHN for dental applications, particularly in remineralization and antibacterial treatments.





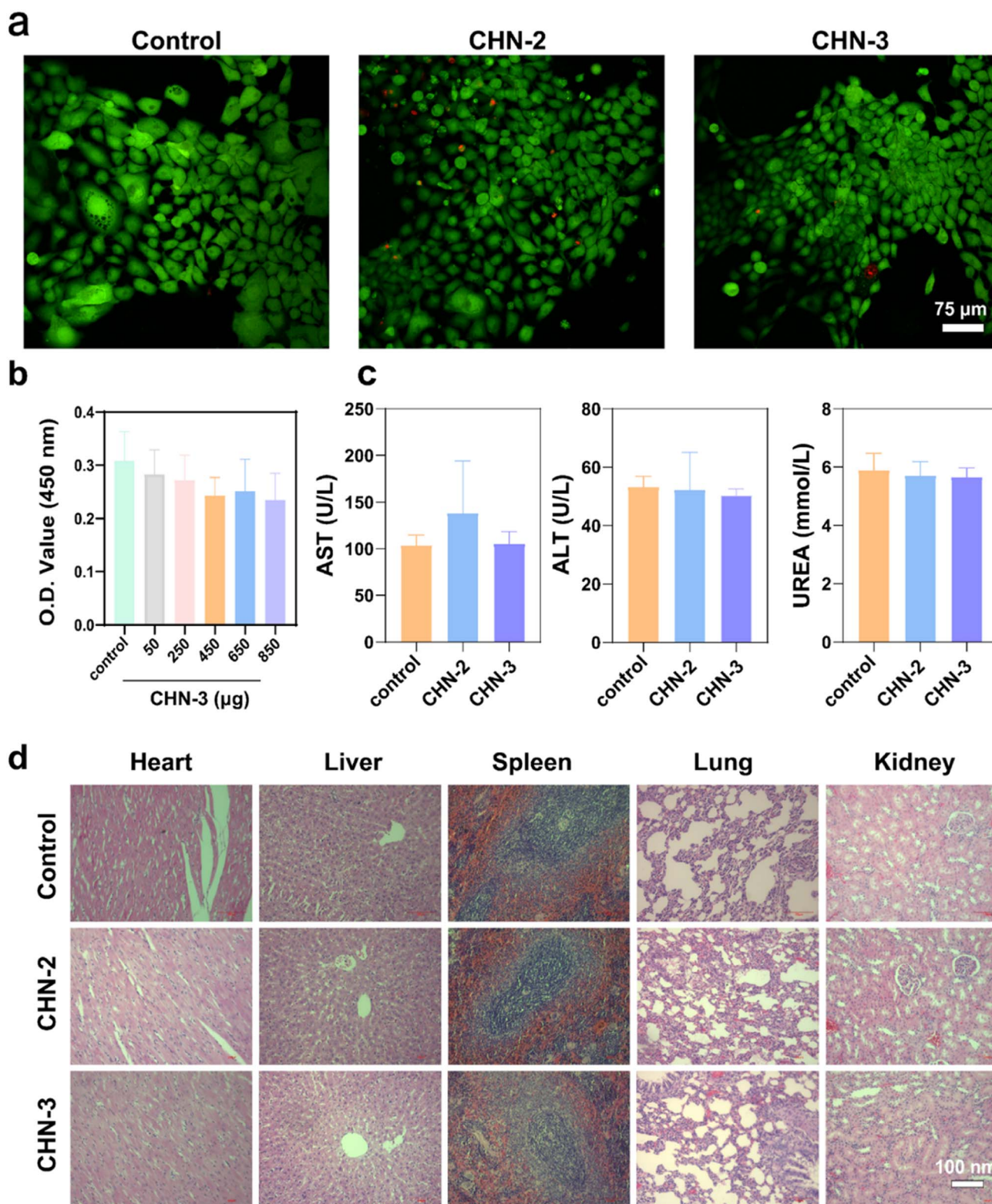


**Fig. 6** Toxicity Assessment. (a) CLSM images assessment of CHN cytotoxicity. (b) Cell viability of HOK treated with different concentrations of CHN. (c) The key hematological parameters in rats treated with CHN and deionized water (d) display H&E-stained histological sections of the heart, liver, spleen, lungs, and kidneys from rats subjected to varying concentrations of CHN *via* gavage, alongside a control group with no drug administration. This aims to evaluate the systemic toxicity of CHN by observing potential histopathological alterations in different organs.





## 4 Conclusion

In this study, a network structure was formed by the cross-linking reaction of sodium tripolyphosphate (TPP) with chitosan to stabilize calcium and phosphate ions. By introducing traditional Chinese medicine components HK-NPs, as well as sodium fluoride, we successfully constructed a CHN composite nanomaterials with efficient antibacterial and remineralization functions. The successful construction of the nanocomposite was demonstrated by FTIR characterization. The results of *in vitro* and *in vivo* experiments showed that CHN nanocomposites could effectively inhibit the growth of common cariogenic bacteria, including *S. mutans*, *S. aureus* and *E. coli*. The inhibition rate of *S. mutans* reached 65.38% in CFU assay, thereby reducing the production of acidic substances and preventing the development of dental caries. CHN nanocomposites effectively promoted remineralization of demineralized enamel through sustained release of calcium, phosphate, and fluoride ions. In particular, combined with nanocoating technology, the remineralization effect of CHN nanocomposites was further enhanced. Compared with other nanocoatings such as PDA and TA-Cu, the combination of TA-Fe and CHN nanocomposites showed the best remineralization effect. In conclusion, the multifunctional composite material presented in this study shows significant advantages in antibacterial and promoting tooth remineralization compared with the traditional single remineralization method, providing an effective new strategy for the prevention and treatment of enamel white spot lesions. In the future, we plan to further explore the potential of this material for the treatment of dentin caries and provide theoretical and experimental basis for the clinical prevention and treatment of dental caries.

## Author contributions

Yuanping Hao: topic selection, ideas, formulation or evolution of overarching research goals and aims, writing and editing. Yanling Yu: acquisition of the financial support, resources, supervision. Lihui Wang: investigation, formal analysis, writing-original draft. Shuqiang Niu: supervision, data curation. Shanshan Xu: visualization, investigation.

## Conflicts of interest

The authors declare no conflicts of interest.

## Acknowledgements

This research was financially supported by the Qingdao Key Health Discipline Development Fund (2022–2024); and Qingdao Clinical Research Center for Oral Diseases (Grant No. 22-3-7-lczz-7-nsh); the Doctor Fund Project of Qingdao Stomatological Hospital (2021BS01). Shandong Provincial Key Medical and Health Discipline of Oral Medicine (Qingdao University Affiliated Qingdao Stomatological Hospital) (2024–2026).

## References

- V. P. Mathur and J. K. Dhillon, *Indian J. Pediatr.*, 2017, **85**, 202–206.
- A. I. Arshad, P. Ahmad, P. M. H. Dummer, M. K. Alam, J. A. Asif, Z. Mahmood, N. A. Rahman and N. Mamat, *Eur. J. Dent.*, 2020, **14**, 128–143.
- L. Sharab, C. Loss, D. Jensen, G. T. Kluemper, M. Alotaibi, H. Nagaoka and Am. J. Orthod, *Dentofacial Orthop.*, 2023, **163**, 835–842.
- M. Khoroushi and M. Kachuie, *Contemp. Clin. Dent.*, 2017, **8**, 11–19.
- K. Lopatiene, M. Borisovaite and E. Lapenaite, *J. Oral Maxillofac. Res.*, 2016, **7**, 1–11.
- M. Sonesson, F. Bergstrand, S. Gizani and S. Twetman, *Eur. J. Orthod.*, 2017, **39**, 116–121.
- D. Sundararaj, S. Venkatachalapathy, A. Tandon and A. Pereira, *J. Int. Soc. Prev. Community Dent.*, 2015, **5**, 433–439.
- E. Zabokova-Bilbilova, L. Popovska, B. Kapusevska and E. Stefanovska, *Pril (Makedon Akad Nauk Umet Odd Med Nauki)*, 2014, **35**, 161–168.
- E. Abou Neel, A. Aljabo, A. Strange, S. Ibrahim, M. Coathup, A. Young, L. Bozec and V. Mudera, *#N/A*, 2016, **11**, 4743–4763.
- D. Elkassas and A. Arafa, *J. Dent.*, 2014, **42**, 466–474.
- L. M. Estes Bright, M. R. S. Garren, M. Ashcraft, A. Kumar, H. Husain, E. J. Brisbois and H. Handa, *ACS Appl. Mater. Interfaces*, 2022, **14**, 21916–21930.
- M. N. Bijle, M. Ekambaram, E. C. Lo and C. K. Y. Yiu, *J. Dent.*, 2020, **99**, 1–28.
- A. Al-Mulla, L. Karlsson, S. Kharsa, H. Kjellberg and D. Birkhed, *Acta Odontol. Scand.*, 2010, **68**, 323–328.
- T. O. Peric, D. L. Markovic, V. J. Radojevic, R. M. Heinemann, B. B. Petrovic and J. S. Lamovec, *J. Appl. Biomater. Funct. Mater.*, 2014, **12**, 234–239.
- M. D. Weir, L. C. Chow and H. H. Xu, *J. Dent. Res.*, 2012, **91**, 979–984.
- A. Brochner, C. Christensen, B. Kristensen, S. Traanaeus, L. Karlsson, L. Sonnesen and S. Twetman, *Clin. Oral Investig.*, 2011, **15**, 369–373.
- N. J. Cochrane, S. Saranathan, F. Cai, K. J. Cross and E. C. Reynolds, *Caries Res.*, 2008, **42**, 88–97.
- A. Alamri, Z. Salloom, A. Alshaia and M. S. Ibrahim, *Molecules*, 2020, **25**, 1–25.
- H. E. Skallevoid, D. Rokaya, Z. Khurshid and M. S. Zafar, *Int. J. Mol. Sci.*, 2019, **20**, 1–24.
- H. O. Simila and A. R. Boccaccini, *Dent. Mater.*, 2022, **38**, 725–747.
- V. P. Varlamov, A. V. Il'ina, B. T. Shagdarova, A. P. Lunkov and I. S. Mysyakina, *Biochemistry*, 2020, **85**, S154–S176.
- C. Ardean, C. M. Davidescu, N. S. Nemes, A. Negrea, M. Ciopec, N. Duteanu, P. Negrea, D. Duda-Seiman and V. Musta, *Int. J. Mol. Sci.*, 2021, **22**, 1–28.
- J. Zhang, V. Boyes, F. Festy, R. J. M. Lynch, T. F. Watson and A. Banerjee, *Dent. Mater.*, 2018, **34**, 1154–1167.



- 24 C. G. Aimoli and M. M. Beppu, *Colloids Surf., B*, 2006, **53**, 15–22.
- 25 J. He, Y. Bao, J. Li, Z. Qiu, Y. Liu and X. Zhang, *J. Dent.*, 2019, **80**, 15–22.
- 26 D. Dai, J. Wang, H. Xie and C. Zhang, *Mater. Today Bio*, 2023, **21**, 1–28.
- 27 M. Fan, M. Li, Y. Yang, M. D. Weir, Y. Liu, X. Zhou, K. Liang, J. Li and H. H. K. Xu, *Dent. Mater.*, 2022, **38**, 1518–1531.
- 28 Y. Zhu, J. Yan, B. M. Mujtaba, Y. Li, H. Wei and S. Huang, *Eur. J. Oral Sci.*, 2021, **129**, 1–11.
- 29 M. Simeonov, A. Gussiyska, J. Mironova, D. Nikolova, A. Apostolov, K. Sezanova, E. Dylulgerova and E. Vassileva, *Eur. Polym. J.*, 2019, **119**, 14–21.
- 30 Z. Xiao, K. Que, H. Wang, R. An, Z. Chen, Z. Qiu, M. Lin, J. Song, J. Yang, D. Lu, M. Shen, B. Guan, Y. Wang, X. Deng, X. Yang, Q. Cai, J. Deng, L. Ma, X. Zhang and X. Zhang, *Dent. Mater.*, 2017, **33**, 1217–1228.
- 31 W. Yang, J. Fu, T. Wang and N. He, *J. Biomed. Nanotechnol.*, 2009, **5**, 591–595.
- 32 Y. Xiong, Y. X. Feng, M. Chang, Q. Wang, S. N. Yin, L. Y. Jian and D. F. Ren, *J. Sci. Food Agric.*, 2023, **103**, 3447–3456.
- 33 A. Pistone, A. de Gaetano, E. Piperopoulos and C. Abate, *Materials*, 2023, **16**, 1–13.
- 34 S. F. Hosseini, M. R. Soleimani and M. Nikkhah, *Int. J. Biol. Macromol.*, 2018, **111**, 730–737.
- 35 D. Lu, F. Li, C. Zhao, Y. Ye, X. Zhang, P. Yang and X. Zhang, *J. Dent. Res.*, 2023, **102**, 1315–1325.
- 36 H. Tebyaniyan, A. Hussain and M. Vivian, *Future Microbiol.*, 2023, **18**, 825–844.
- 37 L. Li, C. Chen, C. Zhang, R. Luo, X. Lan, F. Guo, L. Ma, P. Fu and Y. Wang, *J. Mater. Chem. B*, 2021, **9**, 9770–9783.
- 38 A. E. Solinski, C. Ochoa, Y. E. Lee, T. Paniak, M. C. Kozlowski and W. M. Wuest, *ACS Infect. Dis.*, 2018, **4**, 118–122.
- 39 S. Tao, X. Yang, L. Liao, J. Yang, K. Liang, S. Zeng, J. Zhou, M. Zhang and J. Li, *Dent. Mater.*, 2021, **37**, 1337–1349.
- 40 K. C. Chiu, Y. H. Shih, T. H. Wang, W. C. Lan, P. J. Li, H. S. Jhuang, S. M. Hsia, Y. W. Shen, M. Yuan-Chien Chen, T. M. Shieh and J. Formosan, *Med. Assoc.*, 2021, **120**, 827–837.
- 41 C. Ochoa, A. E. Solinski, M. Nowlan, M. M. Dekarske, W. M. Wuest and M. C. Kozlowski, *ACS Infect. Dis.*, 2019, **6**, 74–79.
- 42 R. Yu, Y. Zou, B. Liu, Y. Guo, X. Wang and M. Han, *Colloids Surf., B*, 2019, **177**, 1–10.
- 43 W. Wu, L. Wang, L. Wang, Y. Zu, S. Wang, P. Liu and X. Zhao, *Int. J. Nanomed.*, 2018, **13**, 5469–5483.
- 44 Y. Guo, Y. Zhao, T. Wang, S. Zhao, H. Qiu, M. Han and X. Wang, *J. Mater. Chem. B*, 2017, **5**, 697–706.
- 45 L. Zhang, Q.-L. Li and H. M. Wong, *Composites, Part B*, 2022, **233**, 1–16.
- 46 Y. Z. Zhou, Y. Cao, W. Liu, C. H. Chu and Q. L. Li, *ACS Appl. Mater. Interfaces*, 2012, **4**, 6901–6910.
- 47 M. P. Ko and C. J. Huang, *Colloids Surf., B*, 2020, **187**, 1–9.
- 48 X. Li, P. Gao, J. Tan, K. Xiong, M. F. Maitz, C. Pan, H. Wu, Y. Chen, Z. Yang and N. Huang, *ACS Appl. Mater. Interfaces*, 2018, **10**, 40844–40853.
- 49 J. Kong, T. He, C. Liu and J. Huang, *Ecotoxicol. Environ. Saf.*, 2022, **231**, 1–18.
- 50 J. Nie, W. Cheng, Y. Peng, G. Liu, Y. Chen, X. Wang, C. Liang, W. Tao, Y. Wei, X. Zeng and L. Mei, *Drug Delivery*, 2017, **24**, 1124–1138.
- 51 W. Cheng, J. Nie, L. Xu, C. Liang, Y. Peng, G. Liu, T. Wang, L. Mei, L. Huang and X. Zeng, *ACS Appl. Mater. Interfaces*, 2017, **9**, 18462–18473.
- 52 J. A. Chapman, W. E. Roberts, G. J. Eckert, K. S. Kula, C. González-Cabezas and Am. J. Orthod, *Dentofacial Orthop.*, 2010, **138**, 188–194.
- 53 J. He, J. Yang, M. Li, Y. Li, Y. Pang, J. Deng, X. Zhang and W. Liu, *ACS Nano*, 2022, **16**, 3119–3134.

